ELSEVIER

Contents lists available at ScienceDirect

Journal of Non-Crystalline Solids

journal homepage: www.elsevier.com/locate/jnoncrysol





Effect of nitrogen on the structure evolution and biological properties of mesoporous bioactive glass nanospheres: Experiments and simulations

Cuilian Wen ^{a,*}, Jiamin Qian ^a, Lijin Luo ^b, Jihong Zeng ^a, Baisheng Sa ^{a,*}, Xuan Zhan ^c, Jian Wang ^{d,e,*}, Liyuan Sheng ^e, Yufeng Zheng ^e

- ^a Multiscale Computational Materials Facility, and Key Laboratory of Eco-materials Advanced Technology, College of Materials Science and Engineering, Fuzhou University, Fuzhou 350100, China
- ^b Fujian Institute of Microbiology, Fuzhou 350007, China
- ^c Fujian Key Laboratory of Oral Diseases & Fujian Provincial Engineering Research Center of Oral Biomaterial & Stomatological Key Laboratory of Fujian College and University, School and Hospital of Stomatology, Fujian Medical University, Fuzhou 350002, China
- ^d College of Mechanical Engineering, Yangzhou University, Yangzhou 225127, China
- ^e Shenzhen Institute, Peking University, Shenzhen 518057, China

ARTICLE INFO

Keywords:
Mesoporous bioactive glass
Nitrogen
Ab initio molecular dynamics simulation
Sol-gel method
Cytotoxicity

ABSTRACT

Mesoporous bioactive glasses (MBGs) have displayed great potential in dental restorations and bone regeneration for their controllable structure and great bioactivity. In this work, we have systematically investigated the effect of nitrogen on structure evolution, apatite-forming ability and cytotoxicity in MBG by successfully preparing the N-containing MBG nanospheres by a modified sol-gel method. It is interesting to demonstrate that all obtained samples exhibit uniform interstitial mesoporous nanospheres microstructure, with the particles size increases as the nitrogen addition increases from 5 to 15 mol.%. Notably, a large amount of blooming flower-like hydroxyapatite deposited on the surface of 15N-MBG after immersed in simulated body fluid for 7 days, exhibiting excellent apatite-forming ability. It is highlighted that the incorporation of nitrogen can stimulate cell proliferation at early incubation time. Moreover, all the MBGs have no obvious inhibitory impact on the hPDLCs growth at extracted concentration. Furthermore, via glass network connectivity analysis from molecular dynamics simulations, the decrease of network connectivity caused by the incorporation of nitrogen could provide looser glass network and higher bioactivity, which explains the experimental results well.

1. Introduction

Since the first developed 45S5 bioglass by Larry L. Hench in 1969 [1], bioactive glasses (BGs) have aroused extensive attentions due to their excellent bioactivity and osteogenic effects, which can apply in biomedical applications such as dental restorations, bone regeneration and drug delivery [2–4]. Compared with melt-quenching method, bioglasses synthesized by sol-gel method exhibit higher bioactivity due to their homogeneous chemical composition and potential mesoporous structures [5–8]. Considerable works show that BGs possess excellent bioactivity behavior because they can rapidly deposit bone-like hydroxyapatite (HA) layers on their surface through chemical reactions when in contact with physiological fluids, which provides them strong bonding with bone tissue [9]. Furthermore, mesoporous bioactive glasses (MBGs) with controllable structure such as fibers and spheres,

can further promote the bioactivity for their large surface area, well dispersity and tunable porosity [10-14].

Recently, various additions have been incorporated into BGs, such as boron [9, 15], strontium [16], silver [17, 18], magnesium [19] and nitrogen [20, 21], etc., to improve the bioactivity, antimicrobial and cell culture properties. Furthermore, previous studies have demonstrated that the biological behavior of MBGs can be improved by including additional therapeutic ions. For example, B₂O₃-containing MBGs can promote its conversion to HA layer and the proliferation of MC3T3-E1 cells [9, 22]. Zn substituted MBG scaffolds allowed a controlled zinc release, which greatly influences the osteoblast cell development, showing in vitro antibacterial capacity [23, 24]. Moreover, Rubidium-containing MBG scaffolds support angiogenesis, osteogenesis related gene expression of hBMSCs and antibacterial activity [25]. It is noteworthy that the surface nitridation can improve the bone cell

E-mail addresses: clwen@fzu.edu.cn (C. Wen), bssa@fzu.edu.cn (B. Sa), jian.wang@yzu.edu.cn (J. Wang).

^{*} Corresponding authors.

response for the melt-derived porous bioactive silicate/borosilicate glass composite scaffolds (ICIE16/BSG) via a nitridation process with hot gas N₂/ammonia at 550 °C, which displayed a quicker degradation rate and high HA superficial layer formation [21]. Moreover, the nitrogen-rich PVD silicon nitride can not only stimulate cellular proliferation but also show antipathogenic efficacy [26]. Additionally, the incorporation of nitrogen to oxynitride bioglasses exhibited their improved physical properties, such as hardness and elastic modulus, via flowing N₂ at high temperature (1400 °C), however, there was no significant change in biological activity [27, 28]. The results imply that lower temperature is more conducive to improve the biological activity for nitrogen modified BGs. However, there are still some problems for N-containing BGs, such as the uncontrollable morphology, low bioactivity, especially, the mechanism between glass network structure and biological activity influenced by the incorporation of nitrogen has not been well elucidated. Therefore, it is of great significance to prepare N-containing MBGs with high bioactivity and good dispersion, and further reveal the effect of nitrogen on the structure evolution and biological properties by combining experiments and simulations.

It can be a very effective approach to design new bioactive glasses and analysis the relevant mechanism by the integrated experimental and simulations studies. Recently, molecular dynamics (MD) simulations have been applied to evaluate the network structure and bioactivity for bioactive glasses at atomic level [29–31]. For instance, the effect of B_2O_3 substitution in SrO-containing BGs has been clarified by molecular dynamic (MD) simulation, displaying an increase in network connectivity (NC) with the increasing incorporation of boron [30]. NC value is an indication of bioactivity for oxide glass, and the glass with higher NC value generally suggest lower dissolution, which further devotes to weaker bioactivity [32, 33]. However, to the best of our knowledge, there is rarely simulation study conducted on N-containing bioactive glasses.

In this work, N-containing MBG nanospheres based on $60 \text{SiO}_2 - 30.8 \text{Ca} - 9.2 \text{P}_2 \text{O}_5$ (mol.%, Ca/P = 1.67) system were synthesized by a modified sol-gel method employing surfactant. The effect of nitrogen incorporation on structural evolution, apatite-forming ability and cytotoxicity were systematically investigated by experiments. Furthermore, we utilized *ab initio* molecular dynamic simulations to understand the atomic-level structure evolution of glasses, with the experimental studies, to reveal the relationship of the network structure and bioactivity of N-containing bioactive glasses.

2. Experimental

2.1. Materials preparation

Tetraethyl orthosilicate (TEOS), triethyl phosphate (TEP), calcium nitrate tetrahydrate (CN), ethyl acetate (EA), ethanol absolute (EtOH) and ammonium hydroxide (1 M NH $_4$ OH) were purchased from Sinopharm Reagent Co. Ltd. (Beijing, China). Hexadecy Itrimethyl ammonium bromide (CTAB) was supplied by Macklin (Shanghai, China). Ethylenediamine ($C_2H_8N_2$) were provide from Aladdin (Shanghai, China). All chemical reagents above were analytical grade. Deionized water (DW) was obtained from a water purification system (Milipore S. A.S., France).

2.2. Bioglasses synthesis

In this research, we synthesize N-containing MBG samples based on $60 \text{SiO}_2 – 30.8 \text{CaO} - 9.2 \text{P}_2 \text{O}_5$ (mol.%, Ca/P = 1.67) systems by modified sol-gel method with templates. Herein, we use TEOS, CN and TEP as the precursors of SiO_2 , CaO and $\text{P}_2 \text{O}_5$, and $\text{C}_2 \text{H}_8 \text{N}_2$ as nitrogen source, respectively. Firstly, 0.7 g CTAB was dissolved in 33 mL DW under magnetic stirring at ambient temperature until the solution became transparent completely, and then 10 mL of EA was added into the solution for 30 min stirring with micro-emulsion droplets formed. After

that, 7 mL NH₄OH (1 mol/L) was added by injected dropwise as template corrodent and hydrolysis catalyst. After stirring for 15 min, 3.6 mL TEOS, 0.95 mL TEP and 2.089 g CN were sequentially added into the above mixture in every 30 min interval. The resultant solution was vigorously stirred for another 3 h to obtain white suspensions. The white precipitate was collected by centrifugation, rinsed with EtOH and DW for 3 times in turn, then dried at 60 °C for 24 h to get dried gel. Finally, the samples were calcined at 600 °C under air to remove surfactants and nitrates. For N-containing MBG samples, different amount of $\rm C_2H_8N_2$ was added to the mixture after adding NH₄OH for 15 min. According to the molar ratio of nitrogen concentration in the glass, the samples were denoted as MBG, 5N-MBG and 15N-MBG, respectively. The corresponding compositions of prepared samples are listed in Table 1.

2.3. Characterization of bioglasses

The obtained samples before and after immersed in SBF solution were characterized by XRD (Miniflex 600, Rigaku, Japan) analysis, operated under Cu-K α radiation (wavelength of 0.15418 nm) with 20 angle from 10° to 70° at a scan speed of 4 $^{\circ}$ /min. The functional groups of the corresponding samples were characterized by FTIR spectroscopy (Nicolet-5700, Thermo, America) using 100 mg KBr mixed with 1 mg glass powder during the range of 400–4000 cm $^{-1}$. The surface morphology of the samples was detected by SEM (SUPRA-55, Zeiss, Germany) and TEM (Jem-2100F, Jeol, Japan) analyses. The N_2 adsorption-desorption isotherms of the samples were measured by a surface and micropore size analyzer (3flex, Micromeritics, America) to determine the textural properties using Brunauer-Emmett-Teller (BET) and Barrett-Joyner-Halanda (BJH) methods. The samples were degassed at 250 $^{\circ}$ C under vacuum for 3 h to remove moisture and other contaminants before testing.

2.4. In vitro bioactivity test

The immersion test in simulated body fluid (SBF) was introduced to investigate in vitro bioactivity of the prepared BGs. The SBF solution was prepared according procedures of Kokubo [34] by dissolving quantitative NaCl, NaHCO₃, KCl, K₂PHO₄•3H₂O, MgCl₂•6H₂O, CaCl₂ and NaSO₄ in DW, with the pH value equal to 7.4 by slowly adjusting with 1 M HCl and Tris at 37 °C. The pressed samples with the size of $\Phi10~\text{mm}\times2~\text{mm}$ were immersed in SBF solution with a concentration ratio of 1.5 mg/ml in a water bath kept at 37 °C for 7 days. To ensure the ion concentration was consistent with that in the physiological environment, the solution was replaced every 2 days. The samples after SBF immersion were investigated by XRD, FTIR and SEM analyses.

2.5. Cell cultivation and cytotoxicity analysis

The human periodontal ligament cells (hPDLCs) were cultivated in Alpha-Modified Eagle's Medium ($\alpha\text{-MEM}$) containing 10% fetal bovine serum (FBS) in an incubator at 37 °C with an atmosphere containing 5% CO $_2$. The BG powders were sterilized at 121 °C for 20 min for autoclaving, then added into serum-free $\alpha\text{-MEM}$ medium at a concentration rate of 1 mg/ml, mixed for 24 h on a 37 °C shaker. Subsequently, the extracted solution was further diluted to 0.05, 0.1, 0.2, 0.4 and 0.8 mg/mL. The hPDLCs were placed in a 96-well plate at a density of 5×10^4 cells per well and incubated for 24 h to allow cell adhesion. After the removal of supernatant, cell culture medium was replaced with different

Table 1The compositions (mol.%) of the prepared N-containing MBG samples.

Sample	SiO_2	CaO	P_2O_5	N
MBG	60	30.8	9.2	0
5N-MBG	60	30.8	9.2	5
15N-MBG	60	30.8	9.2	15

concentration of glasses extraction and cultured for 1, 3 and 7 days. The cells grown in original medium without any glass was denoted as control group.

The proliferation of hPDLCs was evaluated by a Cell Counting kit-8 (CCK-8, Dojindo, Japan). The wells with cultured cells were rinsed with PBS solution twice, then cultured in 100 μL fresh medium containing 10 μL CCK-8 solution for 2 h. The optical density (OD) value was measured using a microplate spectrophotometer at a wavelength of 450 nm. The cellular morphology was observed at different incubation time of 1, 3 and 7 days. Each experimental group was performed for five times to reduce deviation. All data was processed through One-way ANOVA with a Post Hoc test and expressed as means \pm standard deviation (SD). P-value <0.05 was considered statistically significant.

2.6. Ab initio molecular dynamic details

The detailed structures of BG in atomic grade have been conducted by the Born-Oppenheimer *ab initio* molecular dynamic (AIMD) simulation using Vienna *Ab-initio* Simulation Package (VASP) with a canonical ensemble Nose-Hoover thermostat (NVT) [35, 36]. The calculations inputs and results were dealt with the ALKEMIE platform [37].

The numbers of Si, O, Ca, P and N atoms in the simulation models were listed in Table 2. The fixed density of $2.172~g/cm^3$ was measured according to Pycnometer Test Method. The density is calculated according the equation as follows:

$$\rho = \frac{W_{\text{dry}}}{V_2 - V_1} \tag{1}$$

where W_{dry} is the dry weight of samples, and V_2 - V_1 is the changed volume of water before and after immersion. The glass system was simulated by the simulating melt-quench process, distinguished form experimental method, with a time step of 1.5 fs. The simulated systems were firstly melted at 2000 K for 2000 steps, then quenched to 900 K for 5500 steps, finally kept at 900 K for 4500 steps. We used the final 500 steps to analyze the state vibration density of states (VDOS) through the formula [9]:

$$f(\omega) = \frac{2}{\pi} \int_0^\infty C(t) \cos(\omega t) dt$$
 (2)

where C(t) is the velocity autocorrelation function, and ω is the vibration frequency.

In the glass system, the tetrahedron formed by the atoms (Si/P) are referred to Q_n distribution, where "n" is the number of bridging oxygen atoms which connected to the central atom in tetrahedron. The glass network connectivity (NC) was calculated from the equation [33] as follows:

$$NC_{\text{overall}} = \frac{NC_{\text{Si}} \times [SiO_2] + NC_P \times 2[P_2O_5]}{[SiO_2] + 2[P_2O_5]}$$
(3)

where [x] ($x = SiO_2$, P_2O_5) represents the mol.% ratio of x in different glass system, NC_y (y = Si, P) was calculated by the following equation:

$$NC_{y} = \sum_{n=0}^{4} n \times Q_{n}^{y}. \tag{4}$$

Table 2The number of atoms in different glass systems for AIMD simulations.

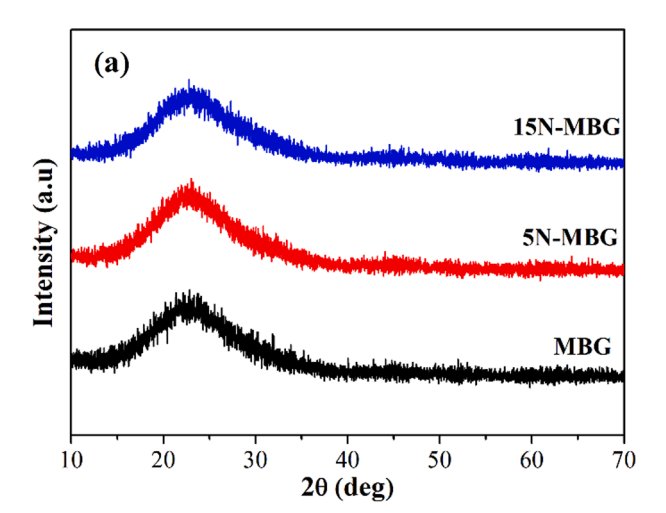
Sample	Si	Ca	P	0	N
MBG	36	18	12	120	0
5N-MBG	36	18	12	140	8
15N-MBG	36	18	12	165	18

3. Results and discussion

3.1. Characterization of the prepared MBGs

The phase structure of MBG samples after calcined at 600 °C were characterized by XRD analyses, as shown in Fig. 1(a). All the samples exhibit a broad peak around $2\theta=15^{\circ}{\sim}35^{\circ}$, which indicates amorphous characteristic of the calcined MBG, 5N-MBG and 15N-MBG samples. Compared with MBG, the incorporation of nitrogen into the glasses does not have a significant effect on the amorphous structure. It should be mentioned that compared with the crystallization structure, the amorphous nature of BGs could be more beneficial for biological activity due to the higher dissolution in physiological fluid [38].

FTIR analysis was carried out to analyze the functional groups of MBG and N-containing MBGs, as shown in Fig. 1(b). The obvious absorption bands at 465 and 1090 cm⁻¹ are attributed to the typical Si-O-Si non-stretching vibration and Si-O-Si symmetrical bending vibration [25, 39]. The peaks observed at 964 cm⁻¹ are belonged to the non-bridging oxygen bonds (Si-O-NBO) [40]. Moreover, the peaks appeared at 800 cm⁻¹ could be related to C—N bending vibration [41, 42], whose intensity increases with increasing nitrogen concentration. It is worth noting that there is gradually increased intensity of the absorption peaks around 1635 and 3440 cm⁻¹ with the increasing nitrogen in BGs, which can be ascribed to N—H stretching overlapped with O—H bond [43, 44], indicating that nitrogen have been successfully incorporated into glass network structure. The OH groups can be related to water absorbed from



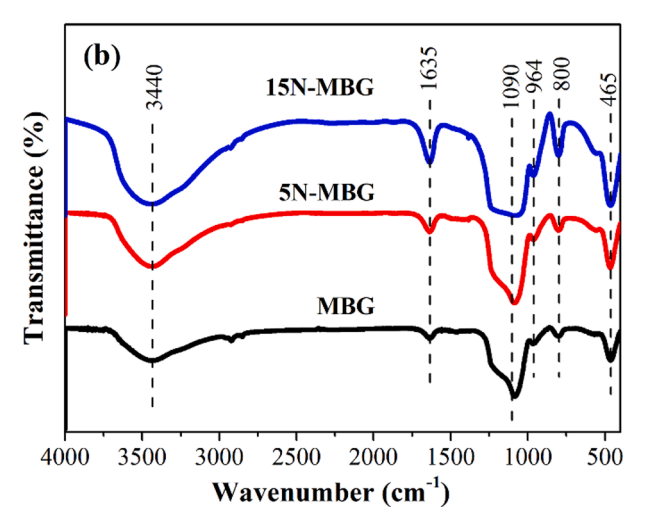


Fig. 1. (a) XRD and (b) FTIR spectra of N-containing MBG samples calcined at $600\ ^{\circ}\text{C}.$

environment, suggesting the prepared glasses are hydrophilic.

Fig. 2 shows the surface morphology of prepared MBGs samples. It is clear that all samples exhibit uniform mesoporous nanospherical microstructure with corrosive pores on their surfaces, derived by modified sol-gel method employing CTAB as surfactant. Moreover, the average particles size is about 70 nm for MBG sample, then significantly increases to about 85 nm for 5N-MBG, and 150 nm for 15N-MBG samples, respectively, as shown in Fig. 2(a)-(c), suggesting that the incorporation of nitrogen has promoted effect on the growth of MBG nanospheres. TEM morphology of N-containing MBG nanospheres was further detected, as shown in Fig. 3(a)-(c). It is obvious that all the samples exhibit nanospheres with radial mesoporous structure after removal of template molecules. The size of nanospheres increases with the increase of nitrogen content, which is consistent with the result observed by SEM. It is clear that the nanospheres of MBG sample is about 70 nm, then significantly increases up to about 150 nm for 15N-MBG samples, which proves that the incorporation of nitrogen can promote the increase of MBG nanospheres and further enhance bioactive properties for their large specific surface area. In addition, SEAD spectra in Fig. 3(d) suggest that 15N-MBG has amorphous feature [34, 45], which

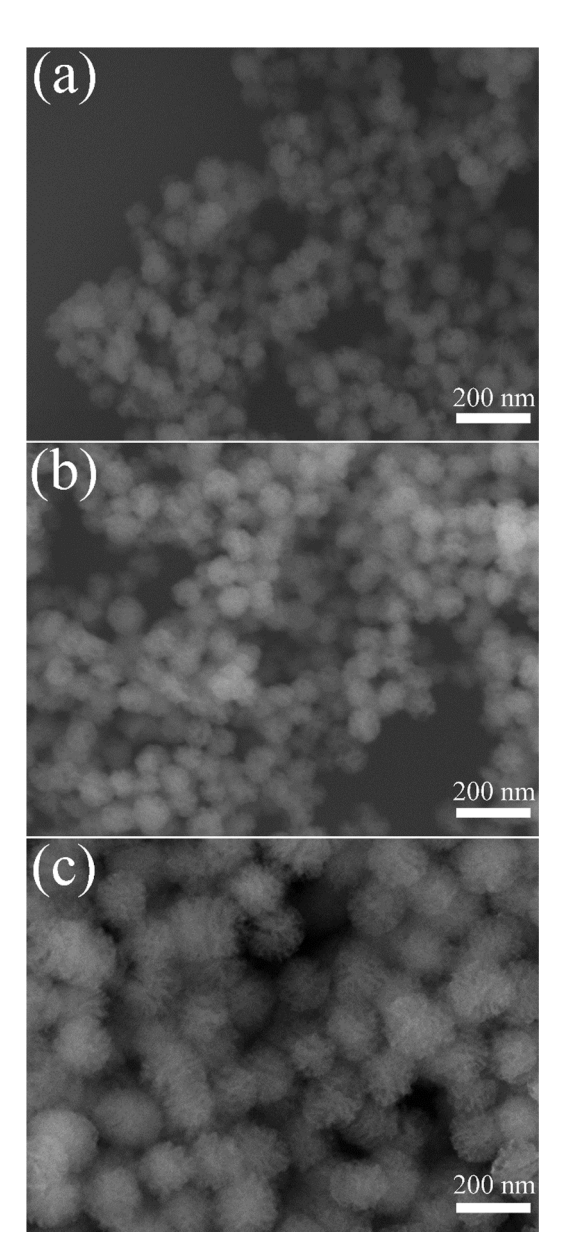


Fig. 2. SEM images of (a) MBG, (b) 5N-MBG, (c) 15N-MBG nanospheres.

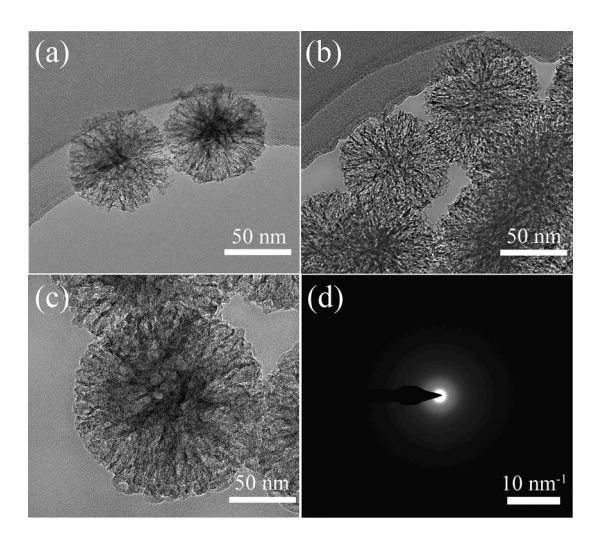


Fig. 3. TEM micrographs of (a) MBG, (b) 5N-MBG, (c) 15N-MBG nanospheres and (d) SAED image of 15N-MBG nanospheres.

is consistent with XRD result.

Fig. 4 represents the schematic illustration of formation process of N-containing MBG nanospheres. Herein, CTAB surfactants form stable spherical micelles through self-assembly, and then combine with EA to form oil-water micro-emulsion droplets as liquid template for mesoporous nanospheres. The aqueous ammonia promotes the hydrolysis and polymerization of TEOS and TEP to form Si-OH silicate oligomers with hydrophilic groups, which continuously arranges in the hydrophilic area of curved interface of the plate emulsion micelles [46, 47]. Here, $\rm C_2H_8N_2$ was used as nitrogen source and incorporated into bioglass during sol-gel process. Finally, the templates were removed by sintering process to obtain N-containing MBG nanospheres with radial mesoporous structure.

The N₂ adsorption-desorption isotherms were performed to analysis the textural properties of MBG in terms of surface area and pore size distribution, as shown in Fig. 5. It exhibits that isotherms are convex upwards in low relative pressure (P/P_0) from Fig. 5(a). On the contrary, the isotherms rise rapidly in the higher P/P₀ area due to the adsorbent underwent capillary condensation. All isotherms are classified as type IV with H3 hysteresis loops, suggesting the mesoporous structure and the presence of slit-shaped pores [46]. Mesoporous structure is confirmed by the pore size distribution in Fig. 5(b). It shows that the pore size of the samples is mostly distributed between 2 and 33 nm. Because the samples exhibit nanospheres with radial mesoporous structure as TEM images in Fig. 3 shown, it is considered that the pore size near the center of nanospheres will be small, while the pore closed to the surface of nanospheres will be large, then the variation range of pore size distribution is reasonable large. In general, pore sizes larger than $100~\mu m$ enable cell seeding, facilitate osteoblast cell proliferation, alkaline phosphatase activity and osteogenic expression [48]. Moreover, nanopores (<2 nm) and mesoporous (2-50 nm) allow biomolecule transportation for any nutrition, waste removal, signaling, and promote adsorption of biological agents and cell [49]. Zhao at al. reported MBG-poly composite scaffolds with pore size around 3.8 nm can stimulate bone regeneration in the calvarial defects [50]. Yun at al. also demonstrated MBG nanospheres with pore size about 28.3 nm could show good cellular viability for J774 cells [51]. Therefore, the pore size distribution of MBG samples in this work could be conducive to promote cellular viability and stimulate bone regeneration. The corresponding values of specific surface area, pore volume and average pore size of the samples by BET and BJH method are listed in Table 3. The specific surface area is 193.24, 225.25 and 271.01 m²/g and the average pore size is 12.66, 11.01 and 8.44 nm for MBG, 5N-MBG and 15N-MBG samples, respectively. It is notably that N-containing MBGs exhibit

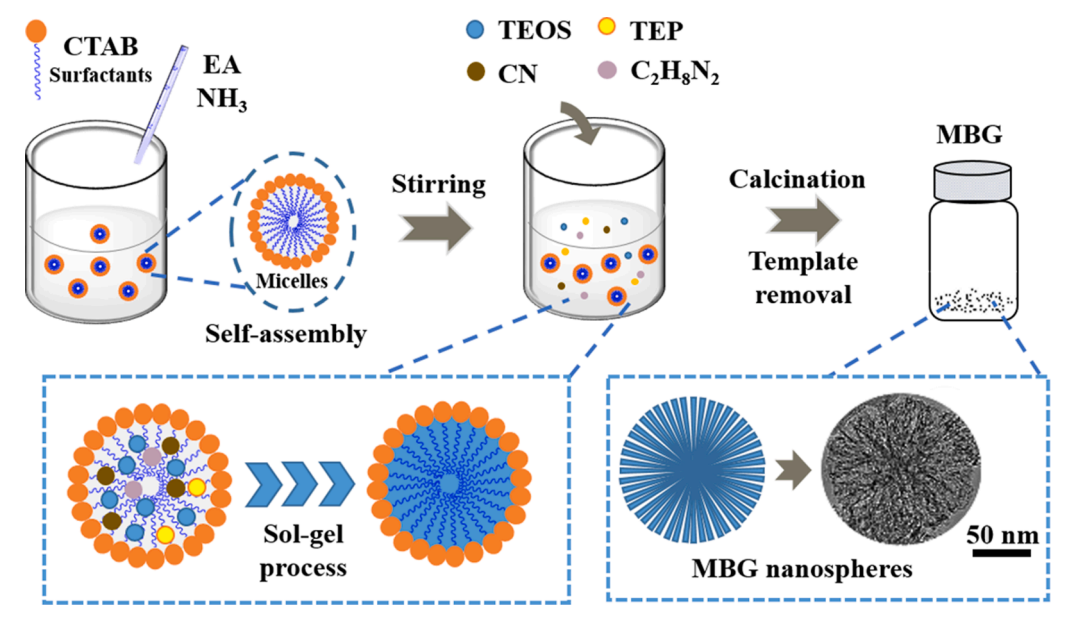


Fig. 4. Schematic representation of the prepared process of N-containing MBG nanospheres.

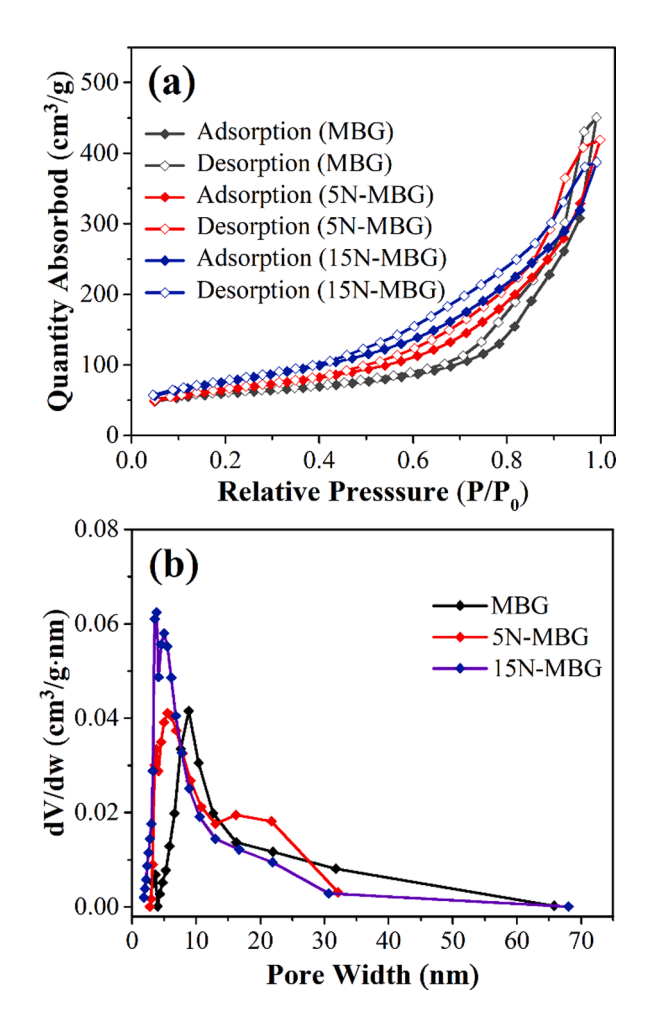


Fig. 5. (a) The N_2 adsorption-desorption isotherms and (b) pore size distribution of N-containing MBG samples.

larger specific surface area than that of MBG, signifying that the addition of nitrogen can significantly improve the textural properties of MBG. Moreover, the large specific surface area with interstitial mesoporous

 $\begin{tabular}{ll} \textbf{Table 3} \\ \textbf{The textural properties of MBG and N-containing MBG samples by BET and BJH method.} \\ \end{tabular}$

Sample	Specific surface area (m²/g)	Pore volume (cm ³ /g)	Average Pore size (nm)
MBG	193.24	0.61	12.66
5N-MBG	225.25	0.62	11.01
15N- MBG	271.01	0.67	8.44

structure for N-containing MBG samples could be helpful for high dissolution ability and excellent biological activity [52].

3.2. In vitro bioactivity assessment

To assess in vitro bioactivity, we investigated the apatite-forming ability by immersing the samples in SBF solution. As shown in Fig. 6 (a)-(c), the surface morphologies of all samples obviously change after immersed in SBF solution for 7 days. The newly uniform depositions on the surface of MBG sample are short rod-like, while thicker deposited layers can be observed on the surface of 5N-MBG and 15N-MBG samples. It is visible that the deposition crystals of 5N-MBG are flake flower-like shape. Moreover, a large amount of sediments aggregates into denser apatite layer on the surface of 15N-MBG sample, looking like blooming flowers with lots of needle-like leaves. It is considered that N-containing MBGs has a higher specific surface area compared with MBG sample, which could provide more HA nucleation sites when immersed in SBF solution. Moreover, the looser glass network connectivity of N-containing MBGs could enhance the ions exchange with SBF solution, resulting in promoted HA crystallization and high bioactivity with finer flower-like HA crystals on bioglass surface. The EDS analysis after immersion in SBF for 7 days is as illustrated in Fig. 6(d)-(f). It is noted that not only the Ca and P content increases but the Ca/P ratio also increases caused by the incorporated nitrogen. The calculated Ca/P atom ratio of the formed apatite precipitates is 1.46, 1.50 and 1.58 for MBG, 5N-MBG and 15N-MBG samples respectively, which is in agreement with literature ranged from 1.3 to 1.7 [53, 54]. The highest Ca/P ratio of 15N-MBG is 1.58, which is quite close to the theoretical value of 1.67 of HA [55], showing excellent bioactive property. The denser HA precipitations owing to incorporated nitrogen can be clearly observed by SEM morphology in comparison with MBG. The results support that the

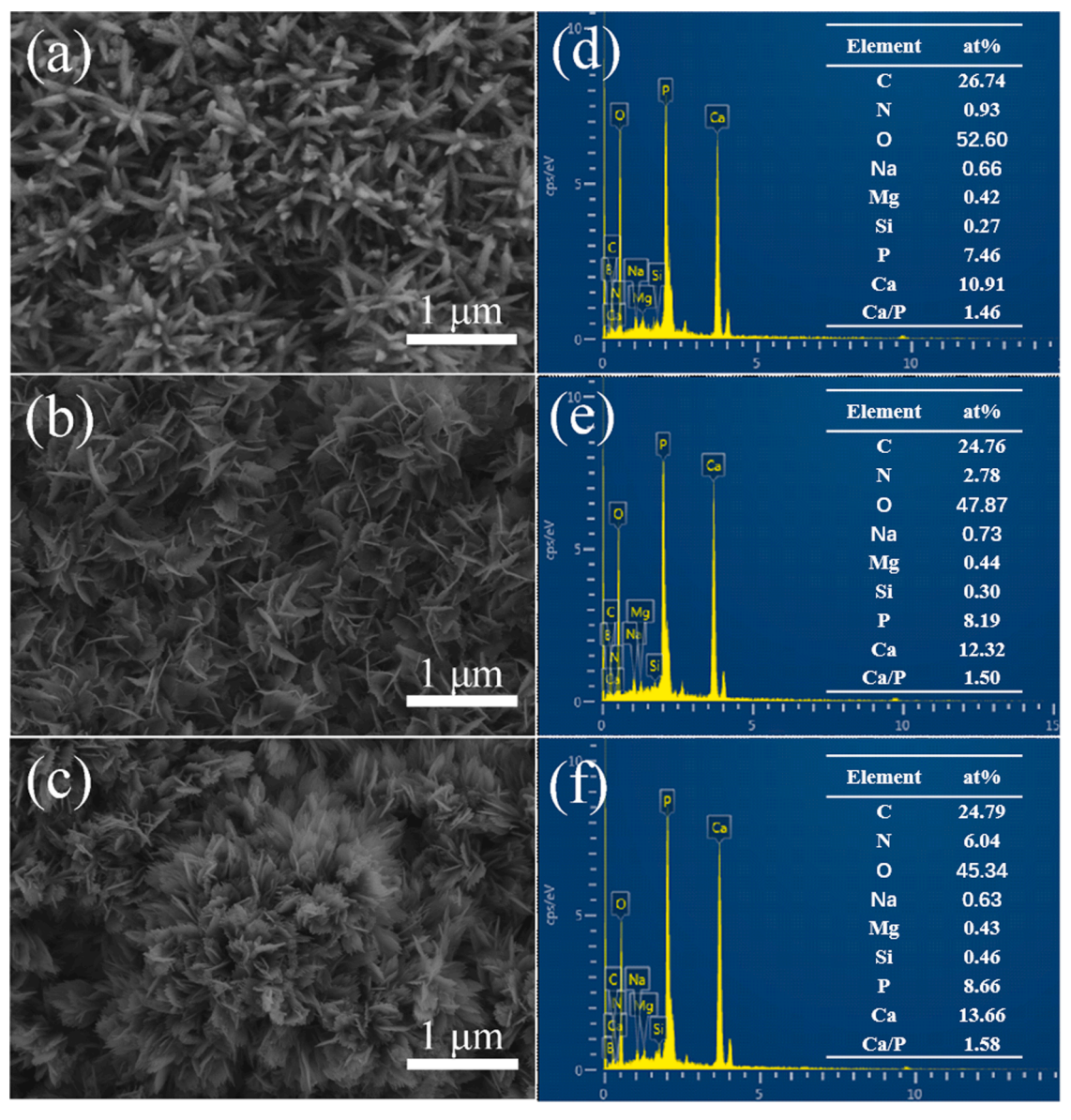


Fig. 6. SEM images and EDS distribution of (a) (d) MBG, (b) (e) 5N-MBG and (c) (f) 15N-MBG after immersed in SBF for 7 days.

incorporation of nitrogen can provide more nucleation sites for ions exchange with SBF solution [56], thereby promote the biomineralization behavior, indicating the enhanced bioactivity of N-containing MBGs.

The deposition on the surface of samples after immersion are further investigated by XRD and FTIR analysis, as shown in Fig. 7. All samples show new diffraction peaks at $2\theta = 25.9^{\circ}$, 31.7° , 34.0° , 39.5° , 46.9° , 53.4° and 49.4° , which are corresponded to HA phase [Ca₁₀(PO₄)₆(OH), (PDF#086-0740)] [57], indicating the deposition of HA on the surface of all samples due to ion exchange with SBF solution. Compared with MBG sample, the intensity of HA diffraction peaks increases with increasing nitrogen in MBG samples, suggesting better bioactivity for N-containing MBG samples. In addition, the diffraction peaks appeared at $2\theta = 21.4^{\circ}$, 23.8° and 26.6° for all samples are identified as SiO₂ [58], which could be ascribed to the broken Si-O-Si and newly-formed Si-OH in glass grid structure, and further polymerizes to form SiO₂ crystalline after immersed in SBF. The intensity of SiO₂ peak of N-containing MBGs is more pronounced in contrast to MBG. The results suggest that the amorphous MBG nanospheres present high dissolution ability, especially, the increased nitrogen in MBG can promote the release of high quantity of Si ions, which combines with -OH in SBF solution and form

more SiO2 crystals.

FTIR spectra of the samples after immersed in SBF are illustrated in Fig. 7(b). All the samples show a double new absorption peaks appeared at 563 and 606 cm⁻¹, ascribed to the P-O bending vibration of the phosphate group [25, 59], which effectively proves the HA deposition on the surface of MBG samples. Moreover, compared with MBGs before SBF immersion, the absorption peaks at 1637 and 3448 cm⁻¹ are identified as the N—H stretching. The peaks located at 800 cm⁻¹ are related to C—N bending vibration, due to the solution of nitrogen ion into SBF solution. The other peaks not mentioned here are similar to FTIR spectra before SBF immersion. These results manifest that HA crystals can be enhanced with the increasing nitrogen in MBG samples, which effectively improves in vitro bioactivity.

3.3. Cytotoxicity evaluation

The cytotoxicity was evaluated by optical density (OD) of hPDLCs incubated in α -MEM medium containing different concentration of MBG samples for 1, 3 and 7 days, as illustrated in Fig. 8. Generally, higher OD value indicates better cell proliferation ability and lower cytotoxicity for biomaterials. It is observed that cell proliferation of all MBG samples

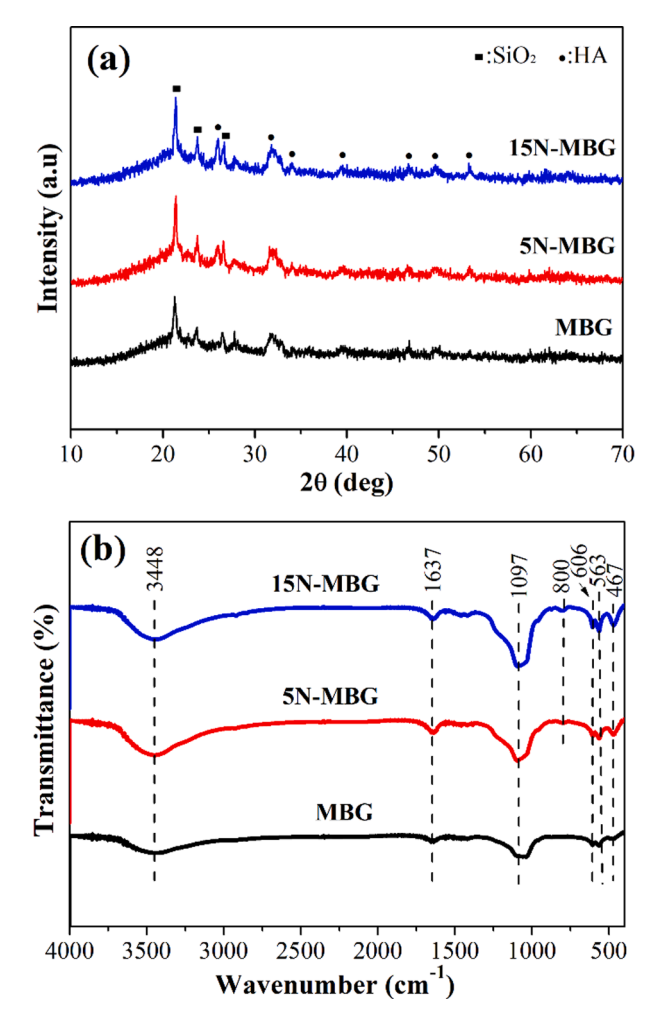


Fig. 7. (a) XRD and (b) FTIR spectra of N-containing MBG nanospheres after immersed in SBF for 7 days.

increases with the increasing incubation time from 1 day to 7 days, indicating that no cytotoxicity is observed for all samples. Compared with control group, the MBG and N-containing MBG groups mostly exhibit higher OD value from 1 to 7 days cultivation, indicating that the medium with MBG powders can provide positive effect on hPDLDs growth, especially for N-containing MBG groups. Only a little inhibition of cell proliferation can be observed on higher extracted concentration (0.8 mg/ml) for MBG group. In addition, higher OD value for N-containing MBG groups suggests the enhanced cell proliferation ability. It is detected that N-containing MBGs significantly promote cell proliferation in the early incubation time, however, the positive effect gradually weakens as the incubation time increases to 7 days, which may ascribe to the higher Si ions released into the medium [60, 61]. Previous study also evaluated that NH2 functionalized MBG scaffolds have no significant toxic effects on bone cell [62]. It is worth noting that 15N-MBG group exhibit excellent cell proliferation even at high extracted concentration of 0.8 mg/ml, suggesting that nitrogen ions release from the glass can improve the cell proliferation to a certain extent [62]. Whereas, other study showed boron-containing MBG with similar BG composition reduced the cell proliferation with 0.8 mg/ml concentration of sample [9]. Moreover, it was reported that NH2-treated BG remarkably increased the concentration of Ca and Si ion in intracellular and in cell culture medium [63], and up-regulated osteogenesis gene expression of hBMSCs both in the presence and absence of biological stimuli [64, 65], which could well explain that N-containing MBGs can enhance cell viability with the increase of nitrogen concentration.

Furthermore, the morphology of hPDLCs incubated in α -MEM

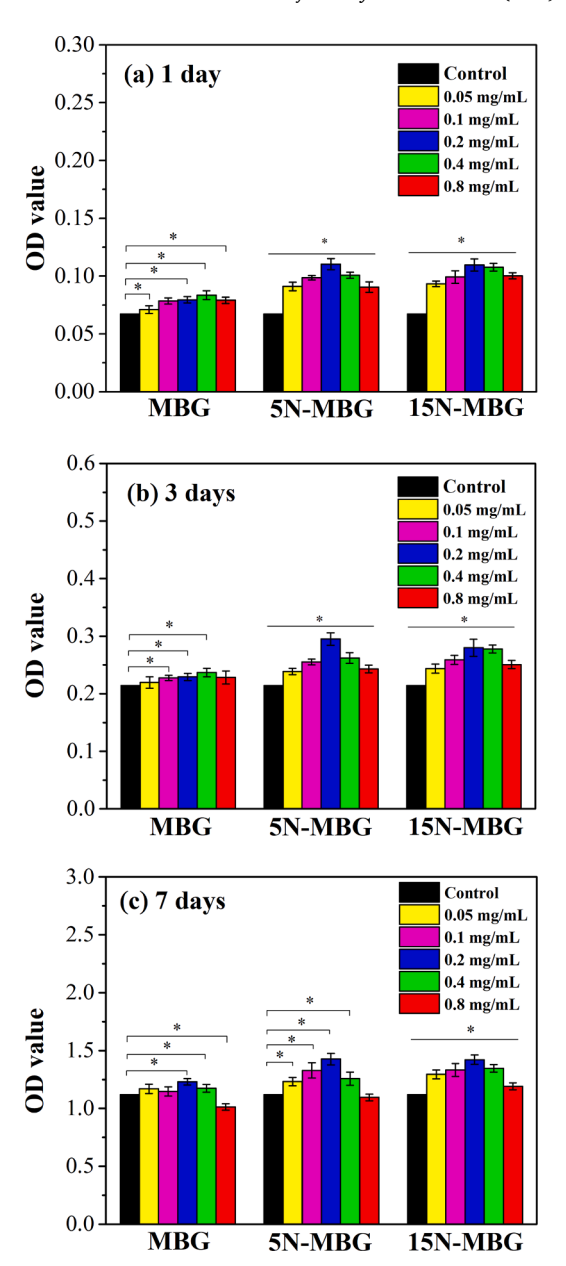


Fig. 8. The optical density of human periodontal ligament cells (hPDLCs) incubated in α -MEM medium with different concentration of N-containing MBG samples for (a) 1, (b) 3 and (c) 7 days. * Statistically significant difference in MBG groups compared with the control group (p<0.05).

medium containing 0.4 mg/ml different samples for 1, 3 and 7 days, as detected in Fig. 9. It is obvious that cell proliferation significantly enhances with the increasing incubation time from 1 day to 7 days for all observed groups, with the typical fibro-blasted morphology for living hPDLCs [66]. Moreover, 15N-MBG sample shows better cell proliferation compared with the other groups, which is consistent with the tendency of OD value. Therefore, our results reveal that all MBG nanospheres have no obvious inhibitory impact on hPDLCs growth at extracted concentration and the incorporation of nitrogen can further promote cell proliferation at the early incubation time.

3.4. Ab initio molecular dynamic simulations

To better understand the relationship of the effect of nitrogen on the structure and bioactivity, AIMD simulations are applied to explore the atomic structure information of N-containing MBG. Fig. 10(a) shows the

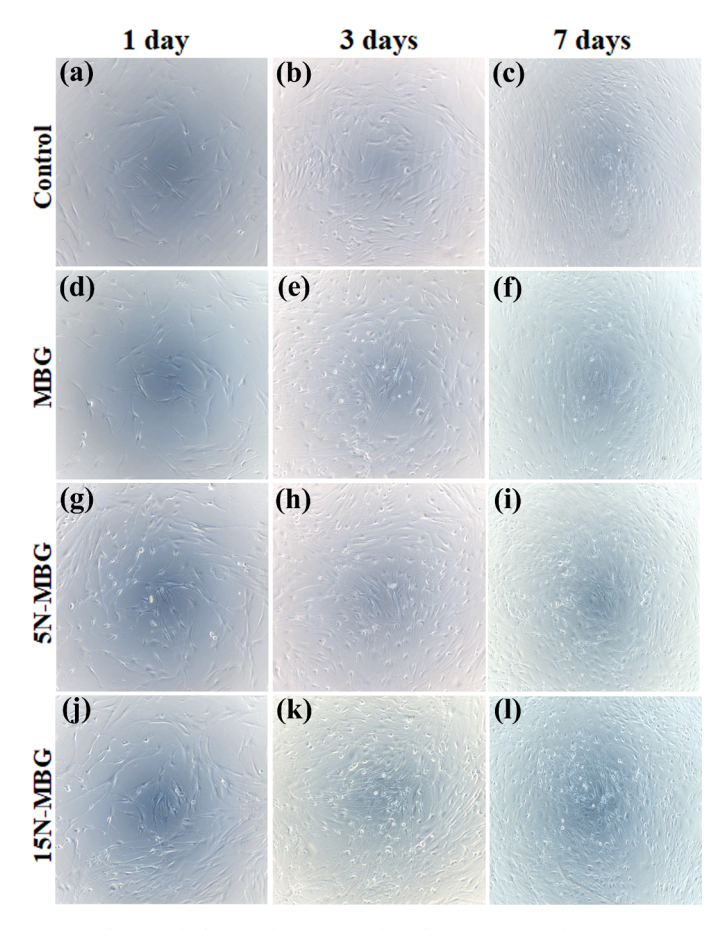


Fig. 9. The morphology of hPDLCs incubated in α -MEM medium containing 0.4 mg/ml different samples for 1, 3 and 7 days: (a-c) control, (d-f) MBG, (g-i) 5N-MBG, (j-l) 15N-MBG.

radial distribution functions (RDFs) and final structure snapshot of simulated 5N-MBG after annealing process. The RDFs of 5N-MBG present the characteristics of short-range order and long-range disorder. which are consistent with the amorphous nature of the samples by XRD analyses. The bonding cutoff distances of P-O and Si-O are fitted around 2.03 and 2.13 Å, respectively. Moreover, the bond angle distributions (BADs) were investigated to analyze the angle inside a polyhedron of glasses, and plots of BADs for simulated 5N-MBG are shown in Fig. 10 (b). Bond angles at the highest intensity peak of both O-Si-O and O-P-O are located around 109°, which are consistent with MD results for 45S5 glass [35] and boron-containing bioglasses [32, 67]. Furthermore, the vibrational feature of the glass was calculated by Eq. (1) at 900 K from Fourier transformation, and the partial simulative vibrational density of state of 5N-MBG is shown in Fig. 10(c). The first low frequency peak located around 100 cm⁻¹ is contributed by the common vibration of all ions [32], which becomes stronger with the nitrogen increases. The second strong peak around 470 cm⁻¹ can be assigned to Si-O-Si symmetrical bending vibration model. It is noted that the peak around 790 cm⁻¹ is belong to bending vibration of nitrogen, well agreed with FTIR results of N-containing MBGs. Additionally, the region between 470 and 780 cm⁻¹ is generally associated with stretching and bending vibrations caused by phosphorous, silicon and oxygen in the tetrahedrons units [29]. No significant change was observed in term of radial distribution functions (RDFs), bond angle distribution (BADs) and vibration density of states (VDOS) for simulated MBG, 5N-MBG and 15N-MBG samples. Herein, we only show the relevant structure information of 5N-MBG.

Moreover, we calculated the average coordination number distribution of Si, Ca, P and N with the increasing nitrogen for simulated MBG samples, as illustrated in Fig. 10(d). Both Si and P as network formers

have stable fourfold coordination with oxygen and remain unchanged with composition for all samples [33]. It is noteworthy that the average coordination numbers of Ca and N increase from 4.94 to 5.79 and 2.07 to 2.58 with increasing nitrogen concentration, respectively. The coordination number of nitrogen is mostly a mixture of ^[2]N and ^[3]N, with the majority of nitrogen ions twofold coordinated for 5N-MBG and threefold coordinated for 15N-MBG respectively. Further, the calculated three-coordinated nitrogen [3]N increases from 25% in 5N-MBG to 66% in for 15N-MBG, while the two-coordinated nitrogen [2]N obviously decreases due to nitrogen increases in MBGs. Consequently, the results speculate that the introduction of nitrogen do not destroy the internal tetrahedral structure of silicate glass, which mutually verifies with experimental analyses. Compared with Si and P, the lower coordinate number of nitrogen is considered to have great effect on glass structure, such as network connectivity, which could promote the dissolution of ions in glass and affect the bioactivity of N-containing MBGs [27].

The glass network connectivity (NC) is an effective measurement to analyze the dissolution and biological activity of glass systems [32]. Table 4 lists the NC value of all glass systems calculated by AIMD simulations. The NC_{Si} of MBG is 2.67 ± 0.02 , which obviously decreases to 2.37 ± 0.02 for 15N-MBG, while the NCn decreases from 1.75 \pm 0.02 for MBG to 1.50 \pm 0.02 for 15N-MBG. Consequently, the NC $_{overall}$ tends to decrease from 2.44 \pm 0.01 to 2.10 \pm 0.03 as nitrogen concentration increases from 0 to 15 mol.%. The results demonstrate that the incorporation of nitrogen has an important effect on the network structure of glass, especially can significantly reduce NC_{Si} and NC_p, and then affect NCoverall value. It was reported that silicate glasses with NC value between 2 and 3 can exhibit good biological activity [33]. The lower NC will provide wider floppy regions, which allows more water molecules penetrate into the glass structure for exchanging ions and promotes the formation of HA [68], which is consistent with the experimental results. The excellent bioactivity for N-containing MBGs could contribute to the increase of non-bridging oxygen atoms and the less-cross-linked glass network by the formation of three-coordinated nitrogen [3]N.

4. Conclusions

In summary, the N-containing MBG nanospheres were successfully prepared by modified sol-gel method employing surfactant, and the effect of nitrogen on the structure and bioactivity was evaluated by combining experimental and AIMD simulations. All the samples exhibit regularly uniform mesoporous nanospherical microstructure with amorphous characteristic, with particles size and specific surface area increase with increasing nitrogen concentration. It is highlighted that 15N-MBG surface has been covered with a large amount of blooming flower-like HA precipitation, indicating that preferable bioactivity for Ncontaining MBGs. All the samples express good cell proliferation and no obvious inhibitory impact on the hPDLCs growth at extracted concentration. Furthermore, the results obtained from AIMD simulations demonstrate that the decrease of NCoverall with the increase of nitrogen, which contributes to good bioactivity for N-containing MBGs. The results illustrate that N-containing MBG nanospheres have excellent biological properties, which have great potential for biomedical applications.

CRediT authorship contribution statement

Cuilian Wen: Conceptualization, Supervision, Writing – original draft. Jiamin Qian: Formal analysis, Methodology, Writing – original draft. Lijin Luo: Data curation, Writing – review & editing. Jihong Zeng: Investigation, Data curation. Baisheng Sa: Conceptualization, Software, Writing – original draft. Xuan Zhan: Validation, Formal analysis. Jian Wang: Writing – review & editing, Validation. Liyuan Sheng: Investigation, Validation. Yufeng Zheng: Writing – review & editing, Conceptualization.

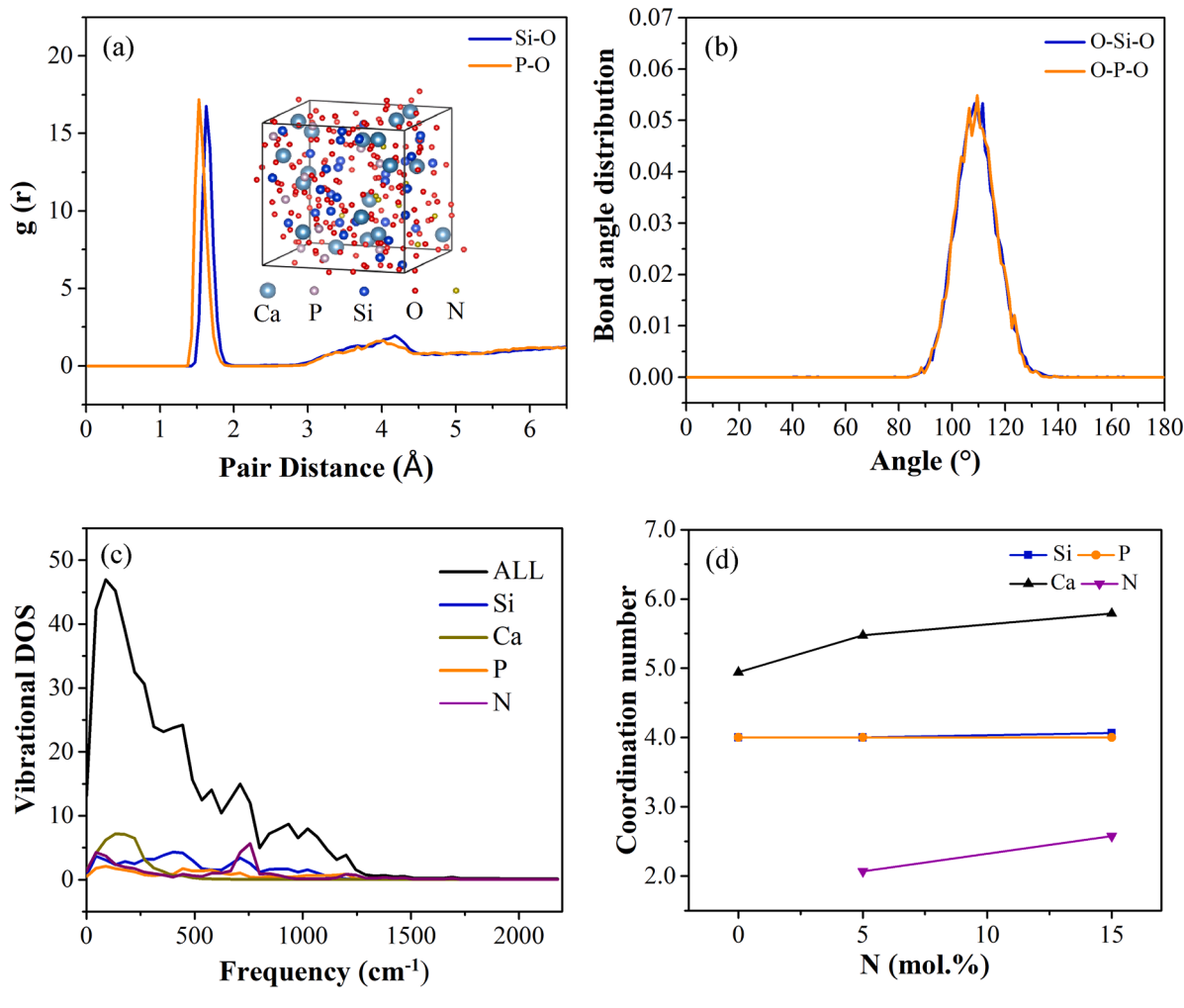


Fig. 10. (a) The radial distribution functions (RDFs) of Si-O and P-O and the structure snapshot of 5N-MBG, (b) the bond angle distributions (BADs) of O-Si-O and O-P-O of 5N-MBG, (c) the vibration density of states (VDOS) of 5N-MBG samples simulated at 900 K, and (d) the average coordination number distribution of Si, Ca, P and N with nitrogen increasing for simulated samples.

Table 4The glass network connectivity (NC) of all glass systems from AIMD simulations.

Sample	NC_{Si}	NC_P	NC _{overall}
MBG	$\textbf{2.67} \pm \textbf{0.02}$	1.75 ± 0.02	2.44 ± 0.01
5N-MBG	2.61 ± 0.02	1.58 ± 0.03	2.33 ± 0.02
15N-MBG	2.37 ± 0.02	1.50 ± 0.02	2.10 ± 0.03

Declaration of Competing Interest

The authors declare no competing financial interest.

Acknowledgements

This work was supported by the National Natural Science Foundation of China (No. 21973012), the Natural Science Foundation of Fujian Province (Nos. 2020J01474, 2020J01351), the Science and Technology Project of Fujian Province (No. 2020N0019), and the "Qishan Scholar" Scientific Research Startup Project of Fuzhou University.

References

[1] O. Kilicoglu, H.O. Tekin, Bioactive glasses and direct effect of increased K_2O additive for nuclear shielding performance: a comparative investigation, Ceram Int. 46 (2020) 1323–1333.

- [2] A. El-Fiqi, N. Mandakhbayar, S.B. Jo, J.C. Knowles, J.H. Lee, H.W. Kim, Nanotherapeutics for regeneration of degenerated tissue infected by bacteria through the multiple delivery of bioactive ions and growth factor with antibacterial/angiogenic and osteogenic/odontogenic capacity, Bioact. Mater. 6 (2021) 123–136.
- [3] Y. Xue, W. Niu, M. Wang, M. Chen, Y. Guo, B. Lei, Engineering a biodegradable multifunctional antibacterial bioactive nanosystem for enhancing tumor photothermo-chemotherapy and bone regeneration, ACS Nano 14 (2020) 442–453.
- [4] L.L. Hench, J.R. Jones, Bioactive glasses: frontiers and challenges, Front. Bioeng. Biotechnol. 3 (2015) 194.
- [5] Z. Nescakova, K. Zheng, L. Liverani, Q. Nawaz, D. Galuskova, H. Kankova, M. Michalek, D. Galusek, A.R. Boccaccini, Multifunctional zinc ion doped sol-gel derived mesoporous bioactive glass nanoparticles for biomedical applications, Bioact. Mater. 4 (2019) 312–321.
- [6] M.S.N. Shahrbabak, F. Sharifianjazi, D. Rahban, A. Salimi, A Comparative Investigation on Bioactivity and Antibacterial Properties of Sol-Gel Derived 58S Bioactive Glass Substituted by Ag and Zn, Silicon 11 (2019) 2741–2751.
- [7] A. Wajda, W.H. Goldmann, R. Detsch, A.R. Boccaccini, M. Sitarz, Influence of zinc ions on structure, bioactivity, biocompatibility and antibacterial potential of meltderived and gel-derived glasses from CaO-SiO₂ system, J Non-Cryst. Solids 511 (2019) 86–99.
- [8] J. Ban, X. Wen, H. Xu, Z. Wang, X. Liu, G. Cao, G. Shao, J. Hu, Dual Evolution in Defect and Morphology of Single-Atom Dispersed Carbon Based Oxygen Electrocatalyst, Adv. Funct. Mater. 31 (2021), 2010472.
- [9] N. Bai, W. Chen, L. Luo, W. Tong, C. Wen, X. Zhan, B. Sa, Effect of B₂O₃ on the structural and in vitro biological assessment of mesoporous bioactive glass nanospheres, J. Am. Chem. Soc. 104 (2021) 3058–3072.
- [10] K. Deshmukh, T. Kovářík, T. Křenek, D. Docheva, T. Stich, J. Pola, Recent advances and future perspectives of sol-gel derived porous bioactive glasses: a review, RSC Adv 10 (2020) 33782–33835.
- [11] M.T. Frassica, S.K. Jones, P. Diaz-Rodriguez, M.S. Hahn, M.A. Grunlan, Incorporation of a silicon-based polymer to PEG-DA templated hydrogel scaffolds for bioactivity and osteoinductivity, Acta Biomater 99 (2019) 100–109.

- [12] Q. Hu, Y. Li, G. Miao, N. Zhao, X. Chen, Size control and biological properties of monodispersed mesoporous bioactive glass sub-micron spheres, RSC Adv 4 (2014) 22678–22687.
- [13] Y. Li, B.P. Bastakoti, Y. Yamauchi, Smart soft-templating synthesis of hollow mesoporous bioactive glass spheres, Chem. Eur. J. 21 (2015) 8038–8042.
- [14] N. Zheng, X. Li, S. Yan, Q. Wang, R. Qiao, J. Hu, J. Fan, G. Cao, G. Shao, Nano-porous hollow Li_{0.5}La_{0.5}TiO₃ spheres and electronic structure modulation for ultrafast H₂S detection, J. Mater. Chem. A 8 (2020) 2376–2386.
- [15] R. Moonesi Rad, A.Z. Alshemary, Z. Evis, D. Keskin, K. Altunbaş, A. Tezcaner, Erratum to: "Structural and biological assessment of boron doped bioactive glass nanoparticles for dental tissue application", Ceram. Int. 44 (2018) 9854–9864.
- [16] S. Amudha, J.R. Ramya, K.T. Arul, A. Deepika, P. Sathiamurthi, B. Mohana, K. Asokan, C.-L. Dong, S.N. Kalkura, Enhanced mechanical and biocompatible properties of strontium ions doped mesoporous bioactive glass, Compos. Part B-Eng. 196 (2020), 108099.
- [17] X. Qin, R. Cao, J. Zheng, G. Shi, L. Ji, A. Zhu, H. Yao, A new strategy for synthesizing silver doped mesoporous bioactive glass fibers and their bioactivity, antibacterial activity and drug loading performance, RSC Adv. 10 (2020) 44835-44840
- [18] A.C. Vale, P.R. Pereira, A.M. Barbosa, E. Torrado, N.M. Alves, Optimization of silver-containing bioglass nanoparticles envisaging biomedical applications, Mater. Sci. Eng. C 94 (2019) 161–168.
- [19] R. Wetzel, O. Bartzok, D.S. Brauer, Influence of low amounts of zinc or magnesium substitution on ion release and apatite formation of Bioglass 45S5, J. Mater. Sci. Mater. Med. 31 (2020) 86.
- [20] Y. Al-Hadeethi, M.S. Al-Buriahi, M.I. Sayyed, Bioactive glasses and the impact of Si₃N₄ doping on the photon attenuation up to radiotherapy energies, Ceram. Int. 46 (2020) 5306–5314.
- [21] F. Orgaz, A. Dzika, O. Szycht, D. Amat, F. Barba, J. Becerra, L. Santos-Ruiz, Surface nitridation improves bone cell response to melt-derived bioactive silicate/ borosilicate glass composite scaffolds, Acta Biomater. 29 (2016) 424–434.
- [22] R.F. Brown, M.N. Rahaman, A.B. Dwilewicz, W. Huang, D.E. Day, Y. Li, B.S. Bal, Effect of borate glass composition on its conversion to hydroxyapatite and on the proliferation of MC3T3-E1 cells, J. Biomed. Mater. Res. A 88 (2009) 392–400.
- [23] C. Heras, S. Sanchez-Salcedo, D. Lozano, J. Pena, P. Esbrit, M. Vallet-Regi, A. J. Salinas, Osteostatin potentiates the bioactivity of mesoporous glass scaffolds containing Zn²⁺ ions in human mesenchymal stem cells, Acta Biomater. 89 (2019) 359–371
- [24] S. Sanchez-Salcedo, S. Shruti, A.J. Salinas, G. Malavasi, L. Menabue, M. Vallet-Regi, In vitro antibacterial capacity and cytocompatibility of SiO₂-CaO-P₂O₅ mesomacroporous glass scaffolds enriched with ZnO, J. Mater. Chem. B 2 (2014) 4836–4847.
- [25] X. He, Y. Liu, Y. Tan, L.M. Grover, J. Song, S. Duan, D. Zhao, X. Tan, Rubidium-containing mesoporous bioactive glass scaffolds support angiogenesis, osteogenesis and antibacterial activity, Mater. Sci. Eng. C 105 (2019), 110155.
 [26] E. Marin, F. Boschetto, M. Zanocco, W. Zhu, T. Adachi, N. Kanamura,
- [26] E. Marin, F. Boschetto, M. Zanocco, W. Zhu, T. Adachi, N. Kanamura, T. Yamamoto, B.J. McEntire, E.N. Jones, C. Powell, J. Hendry, R.M. Bock, B.S. Bal, G. Pezzotti, Biological responses to silicon and nitrogen-rich PVD silicon nitride coatings, Mater. Today Chem. 19 (2021), 100404.
- [27] A. Bachar, C. Mercier, A. Tricoteaux, A. Leriche, C. Follet, M. Saadi, S. Hampshire, Effects of addition of nitrogen on bioglass properties and structure, J. Non-Cryst. Solids 358 (2012) 693–701.
- [28] A. Bachar, C. Mercier, A. Tricoteaux, A. Leriche, C. Follet-Houttemane, M. Saadi, S. Hampshire, Effects of nitrogen on properties of oxyfluoronitride bioglasses, Process Biochem 48 (2013) 89–95.
- [29] X. Lu, L. Deng, P.-.H. Kuo, M. Ren, I. Buterbaugh, J. Du, Effects of boron oxide substitution on the structure and bioactivity of SrO-containing bioactive glasses, J. Mater. Sci. 52 (2017) 8793–8811.
- [30] J. Du, Y. Xiang, Effect of strontium substitution on the structure, ionic diffusion and dynamic properties of 45S5 Bioactive glasses, J. Non-Cryst. Solids 358 (2012) 1059–1071
- [31] M. Montazerian, E.D. Zanotto, J.C. Mauro, Model-driven design of bioactive glasses: from molecular dynamics through machine learning, Int. Mater. Rev. 65 (2019) 297–321.
- [32] X. Lu, L. Deng, C. Huntley, M. Ren, P.H. Kuo, T. Thomas, J. Chen, J. Du, Mixed Network Former Effect on Structure, Physical Properties, and Bioactivity of 45S5 Bioactive Glasses: an Integrated Experimental and Molecular Dynamics Simulation Study, J. Phys. Chem. B 122 (2018) 2564–2577.
- [33] M. Ren, X. Lu, L. Deng, P.H. Kuo, J. Du, B₂O₃/SiO₂ substitution effect on structure and properties of Na₂O-CaO-SrO-P₂O₅-SiO₂ bioactive glasses from molecular dynamics simulations, Phys. Chem. Chem. Phys. 20 (2018) 14090–14104.
- [34] C. Wen, N. Bai, L. Luo, J. Ye, X. Zhan, Y. Zhang, B. Sa, Structural behavior and in vitro bioactivity evaluation of hydroxyapatite-like bioactive glass based on the SiO₂-CaO-P₂O₅ system, Ceram. Int. 47 (2021) 18094–18104.
- [35] J. Yan, Y. Wu, D. Lin, H. Zhan, H. Zhuang, B. Sa, T. Zhang, Structural transformation-induced surface strengthening of borosilicate sealing glass for solid oxide fuel cells, Ceram. Int. 45 (2019) 15629–15635.
- [36] A. Tilocca, Models of structure, dynamics and reactivity of bioglasses: a review, J. Mater. Chem. 20 (2010) 6848–6858.
- [37] G. Wang, L. Peng, K. Li, L. Zhu, J. Zhou, N. Miao, Z. Sun, ALKEMIE: an intelligent computational platform for accelerating materials discovery and design, Comp. Mater. Sci. 186 (2021), 110064.
- [38] Y. Zhang, J. Luan, S. Jiang, X. Zhou, M. Li, The effect of amino-functionalized mesoporous bioactive glass on MC3T3-E1 cells in vitro stimulation, Compos. Part B-Eng. 172 (2019) 397–405.

- [39] H.F. Alazzawi, I.K. Salih, T.M. Albayati, Drug delivery of amoxicillin molecule as a suggested treatment for covid-19 implementing functionalized mesoporous SBA-15 with aminopropyl groups, Drug Deliv. 28 (2021) 856–864.
- [40] J. Ma, C.Z. Chen, D.G. Wang, Y. Jiao, J.Z. Shi, Effect of magnesia on the degradability and bioactivity of sol-gel derived SiO₂-CaO-MgO-P₂O₅ system glasses, Colloid Surf. B 81 (2010) 87–95.
- [41] R. Peymanfar, E. Selseleh-Zakerin, A. Ahmadi, Tailoring energy band gap and microwave absorbing features of graphite-like carbon nitride (g-C₃N₄), J. Alloys Compd. 867 (2021), 159039.
- [42] S. Sadeghian, H. Pourfakhar, M. Baghdadi, B. Aminzadeh, Application of sand particles modified with NH₂-MIL-101(Fe) as an efficient visible-light photocatalyst for Cr(VI) reduction, Chemosphere 268 (2021), 129365.
- [43] Y. Newman Monday, J. Abdullah, N.A. Yusof, S. Abdul Rashid, R.H. Shueb, Facile Hydrothermal and Solvothermal Synthesis and Characterization of Nitrogen-Doped Carbon Dots from Palm Kernel Shell Precursor, Appl. Sci. 11 (2021) 1630.
- [44] H. Zeng, Z. Yu, L. Shao, X. Li, M. Zhu, Y. Liu, X. Feng, X. Zhu, A novel strategy for enhancing the performance of membranes for dyes separation: embedding PAA@ UiO-66-NH₂ between graphene oxide sheets, Chem. Eng. J. 403 (2021), 126281.
- [45] C.-.C. Shih, C.-.S. Chien, J.-.C. Kung, J.-.C. Chen, S.-.S. Chang, P.-.S. Lu, C.-.J. Shih, Effect of surfactant concentration on characteristics of mesoporous bioactive glass prepared by evaporation induced self-assembly process, Appl. Surf. Sci. 264 (2013) 105–110.
- [46] Q. Liang, Q. Hu, G. Miao, B. Yuan, X. Chen, A facile synthesis of novel mesoporous bioactive glass nanoparticles with various morphologies and tunable mesostructure by sacrificial liquid template method, Mater. Lett. 148 (2015) 45–49.
- [47] W. Xie, X. Chen, Y. Li, G. Miao, G. Wang, T. Tian, L. Zeng, X. Chen, Facile synthesis and in vitro bioactivity of radial mesoporous bioactive glass with high phosphorus and calcium content, Adv. Powder Technol. 31 (2020) 3307–3317.
- [48] Y. Zhu, F. Shang, B. Li, Y. Dong, Y. Liu, M.R. Lohe, N. Hanagata, S. Kaskel, Magnetic mesoporous bioactive glass scaffolds: preparation, physicochemistry and biological properties, J. Mater. Chem. B 1 (2013) 1279–1288.
- [49] A. Garcia, I. Izquierdo-Barba, M. Colilla, C.L. de Laorden, M. Vallet-Regi, Preparation of 3-D scaffolds in the SiO₂-P₂O₅ system with tailored hierarchical meso-macroporosity, Acta Biomater 7 (2011) 1265–1273.
- [50] S. Zhao, M. Zhu, J. Zhang, Y. Zhang, Z. Liu, Y. Zhu, C. Zhang, Three dimensionally printed mesoporous bioactive glass and poly (3-hydroxybutyrate-co-3hydroxyhexanoate) composite scaffolds for bone regeneration, J. Mater. Chem. B 2 (2014) 6106–6118.
- [51] H.-s. Yun, S.-h. Kim, S. Lee, I.-h. Song, Synthesis of high surface area mesoporous bioactive glass nanospheres, Mater. Lett. 64 (2010) 1850–1853.
- [52] C. Wu, W. Fan, J. Chang, Functional mesoporous bioactive glass nanospheres: synthesis, high loading efficiency, controllable delivery of doxorubicin and inhibitory effect on bone cancer cells, J. Mater. Chem. B 1 (2013) 2710–2718.
- [53] V. Aina, C. Morterra, G. Lusvardi, G. Malavasi, L. Menabue, S. Shruti, C.L. Bianchi, V. Bolis, Ga-Modified (Si-Ca-P) Sol-Gel Glasses: possible Relationships between Surface Chemical Properties and Bioactivity, J. Phys. Chem. C 115 (2011) 22461–22474.
- [54] Z. Zyman, D. Rokhmistrov, K. Loza, Determination of the Ca/P ratio in calcium phosphates during the precipitation of hydroxyapatite using X-ray diffractometry, Processing Appl. Ceram. 7 (2013) 93–95.
- [55] Y. Liu, K. Xue, S. Yao, Structure, degradation and hydroxyapatite conversion of B-doped 58S bioglass and glass-ceramics, J. Ceram. Soc. Jpn. 127 (2019) 232–241.
- [56] A.J.S. Montserrat Colilla, Maria Vallet-Regi, Amino-Polysiloxane Hybrid Materials for Bone Reconstruction, Chem. Mater. 18 (2006) 5676–5683.
 [57] H. Pirayesh, J.A. Nychka, S. Bose, Sol-Gel Synthesis of Bioactive Glass-Ceramic
- 4555 and its in vitro Dissolution and Mineralization Behavior, J. Am. Ceram. Soc. 96 (2013) 1643–1650.
- [58] T.P. Nguyen, M. Shahedi Asl, S.A. Delbari, A. Sabahi Namini, Q.V. Le, M. Shokouhimehr, M. Mohammadi, Electron microscopy investigation of spark plasma sintered ZrO₂ added ZrB₂–SiC composite, Ceram. Int. 46 (2020) 19646–19649.
- [59] S. Yadav, P. Singh, R. Pyare, Synthesis, characterization, mechanical and biological properties of biocomposite based on zirconia containing 1393 bioactive glass with hydroxyapatite, Ceram. Int. 46 (2020) 10442–10451.
- [60] W. Gong, Z. Huang, Y. Dong, Y. Gan, S. Li, X. Gao, X. Chen, Ionic extraction of a novel nano-sized bioactive glass enhances differentiation and mineralization of human dental pulp cells, J. Endodont. 40 (2014) 83–88.
- [61] H.m. Zhou, Y. Shen, Z.j. Wang, L. Li, Y.f. Zheng, L. Häkkinen, M. Haapasalo, In vitro cytotoxicity evaluation of a novel root repair material, J. Endodont., 39 (2013) 478–483.
- [62] S. Zhao, J. Zhang, M. Zhu, Y. Zhang, Z. Liu, Y. Ma, Y. Zhu, C. Zhang, Effects of functional groups on the structure, physicochemical and biological properties of mesoporous bioactive glass scaffolds, J. Mater. Chem. B 3 (2015) 1612–1623.
- [63] J.H. Lee, M.S. Kang, C. Mahapatra, H.W. Kim, Effect of aminated mesoporous bioactive glass nanoparticles on the differentiation of dental pulp stem cells, PLoS ONE 11 (2016), 0150727.
- [64] J.M. Curran, R. Chen, J.A. Hunt, The guidance of human mesenchymal stem cell differentiation in vitro by controlled modifications to the cell substrate, Biomaterials 27 (2006) 4783–4793.
- [65] D.M.C. Benjamin G. Keselowsky, Andre s J. Garcia, Integrin binding specificity regulates biomaterial surface chemistry effects on cell differentiation, P. Natl. Acad. Sci. USA 17 (2005) 5953–5957.

- [66] P. Han, M. Xu, J. Chang, N. Chakravorty, C. Wu, Y. Xiao, Lithium release from beta-tricalcium phosphate inducing cementogenic and osteogenic differentiation of both hPDLCs and hBMSCs, Biomater. Sci. 2 (2014) 1230–1243.
- [67] Y. Xiang, J. Du, Effect of strontium substitution on the structure of 4585 bioglasses, Chem. Mater. 23 (2011) 2703–2717.
 [68] D.S. Brauer, Bioactive glasses-structure and properties, Angew. Chem. Int. Ed. 54 (2015) 4160–4181.